Nature Photonics **10**, pp. 762-765 (2016)
final version

Real-space coherent manipulation of electrons in a single tunnel junction by single-cycle terahertz electric fields

Katsumasa Yoshioka[1], Ikufumi Katayama[1,*], Yasuo Minami[1], Masahiro Kitajima[1,2], Shoji Yoshida[3], Hidemi Shigekawa[3,*], and Jun Takeda[1,*]

[1]Department of Physics, Graduate School of Engineering, Yokohama National University, Yokohama 240-8501, Japan

[2]LxRay Co. Ltd., Nishinomiya 663-8172, Japan

[3]Faculty of Pure and Applied Sciences, University of Tsukuba, Tsukuba 305-8571, Japan

Abstract: The ultrafast coherent manipulation of electrons using waveform-controlled laser pulses[1-9] is a key issue in the development of modern electronics[10,11]. Developing such an approach for a tunnel junction will provide a new platform for governing ultrafast currents on an ever smaller scale, which will be indispensable for the advancement of next-generation quantum nanocircuits[12-15] and plasmonic devices[16-18]. Here, we demonstrate that carrier-envelope phase controlled single-cycle terahertz electric fields can coherently drive electron tunnelling either from a nanotip to a sample or vice versa. Spatially confined electric fields of more than 10 V/nm strongly modulate the potential barrier at a nanogap in a scanning tunnelling microscope (STM) within a sub-picosecond time scale and can steer a huge number of electrons in an extremely nonlinear regime, which is not possible using a conventional STM. Our results are expected to pave the way for the future development of nanoscale science and technologies.

***e-mail: hidemi@ims.tsukuba.ac.jp; katayama@ynu.ac.jp; jun@ynu.ac.jp**

The latest advances in laser technology have made it possible to control the carrier-envelope phase (CEP) of ultrashort laser pulses with high accuracy. Using few-cycle CEP-controlled near-infrared laser pulses, several studies have demonstrated the ultrafast coherent control of electrons in a wide range of systems[1-9]. In these studies, metallic nanostructures, so-called metal nanotips, were used to produce highly localized near-fields by concentrating laser pulses into dimensions far below the diffraction limit of the incident light. Using a spatiotemporally tuneable near-field of up to ~10 V/nm, ultrafast electron bursts from a nanotip have even been realized[7-9]. These sophisticated electron manipulations will open fascinating avenues for overcoming the bandwidth limitation of signal processing in modern information technology[10,11].

A larger field enhancement is expected to occur at a tunnel junction[12,14,18,19]. The resulting strong nonlinearity will be useful for the manipulation of electrons at the atomic scale, which is highly desirable for the advancement of next-generation integrated nanocircuits[12-15] and plasmonic devices[16-18]. However, strong near-infrared laser pulses focused on a tunnel junction induce thermal expansion[20], leading to permanent damage of the junction. Therefore, precise control of the motion of electrons at the atomic scale is still a challenging task. Recently, single-cycle electric field transients with high intensity have been generated in the terahertz (THz) spectral range (0.1 - 10 THz)[21,22]. In contrast to few-cycle near-infrared laser pulses, single-cycle THz electric fields with a bandwidth over an octave may useful for accurately steering electrons, and can drive electron tunnelling without heating systems because of their low energy. Indeed, THz-field-induced nonlinear electron tunnelling was observed in percolated gold nanostructures[23] and metal-graphene-metal hybrid structures[18] without any thermal effects. THz scanning tunnelling microscopy (THz-STM)[19], which was developed after optical pump-probe STM,[24,25] may allow ultrafast dynamics to be probed with fewer thermal expansion problems.

Here, we demonstrate real-space coherent manipulation of the motion of electrons in a single tunnel junction by utilizing CEP-controlled single-cycle THz electric fields via the Gouy phase shift[26]. Unlike the imaging of surfaces at the atomic scale using conventional STM, our THz-STM with the tunnel junction presented here acts as an ultrafast rectifying diode or a THz-field-effect transistor[7,27]; the electron current is switched on and off via the CEP-controlled single-cycle THz electric fields. The basic

concept of our experimental setup is illustrated in Figs. 1a-1c. Intense single-cycle THz electric field transients were generated by optical rectification of femtosecond laser pulses in a $LiNbO_3$ prism using a tilted-pulse-front configuration[21]. The generated THz pulses were guided into one of two optical paths: one was used for characterizing the THz waveforms by electro-optic sampling (EOS), while the other was used for delivering the THz pulses to a single tunnel junction. The THz pulses were focused onto the apex of a Pt/Ir nanotip. We used highly oriented pyrolytic graphite (HOPG) as a sample because of its atomically flat surface. All measurements were performed under ambient laboratory conditions. By placing either a pair of spherical or cylindrical lenses in the beam path (Fig. 1b), the CEP of the incident THz pulses ($\phi_{CEP} = 0$) was shifted by $\phi_{CEP} = \pi$ or $\phi_{CEP} = \pi/2$, respectively, via the Gouy phase shift. As schematically shown in Fig. 1c, the CEP-controlled single-cycle THz electric field modifies the potential barrier between a nanotip and sample, leading to the unidirectional coherent motion of electrons. Under the irradiation of THz pulses with $\phi_{CEP} = 0$ (Fig. 1d) at the junction, a series of tunnel currents were synchronously generated with the repetition rate of the laser system (1 kHz), as shown in Fig. 1e. Note that the time-integrated value of each current pulse represents the number of rectified electrons driven by a single THz pulse through the junction (see Supplementary Information I).

The CEP dependence of the tunnel current was measured with different CEPs of $\phi_{CEP} = 0$, $\pi/2$, and π, while sweeping the DC bias from 300 mV to -300 mV (Figs. 2a and 2b). The most remarkable feature in Fig. 2b is a series of THz-induced pulse trains, which is a fingerprint of the ultrafast current bursts in the tunnel junction. In the case of $\phi_{CEP} = 0$, the pulse train takes a positive value, which corresponds to an electron tunnelling from the nanotip to the sample. The intensity of the pulse train increases with increasing DC bias. In the case of $\phi_{CEP} = \pi$, on the other hand, the tunnel current shows completely the opposite behaviour; the pulse train with a negative value indicates an electron tunnelling from the sample to the nanotip. In the case of $\phi_{CEP} = \pi/2$, the direction of electron tunnelling strongly depends on the DC bias; electrons undergo tunnelling from the nanotip to the sample under a positive DC bias and in the opposite direction under a negative DC bias. The current pulse disappears as the DC bias approaches 0 (see Supplementary Information II). As schematically summarized in Fig. 2c, the coherent motion of electrons at the junction is controlled by the CEP-locked THz

pulses with a given DC bias.

Figure 2d shows the number of rectified electrons induced by a single THz pulse as a function of the peak electric field with different CEPs ($\phi_{CEP} = 0$ and $\phi_{CEP} = \pi$). The nonlinear increase in the number of rectified electrons with the THz electric field was numerically evaluated on the basis of the Simmons model[28] assuming a potential barrier between the nanotip (M_1) and sample (M_2) under a bias voltage of V, as illustrated in Fig. 2e. As shown by the dashed line in Fig. 2d, the experimental data is accurately reproduced with the adjustable parameters of an effective work function of 3.8 ± 0.1 eV, a gap width of 1.00 ± 0.01 nm, and an enhancement factor of 100,000 ± 10,000. These values were also confirmed by I-Z (current vs. distance) and DC I-V (current vs. voltage) experiments (see Supplementary Information III). This huge field enhancement originates from the extremely tight focusing of the THz electric field onto the single junction with a 1 nm gap induced by the broadband antenna effect of the nanotip and/or the plasmonic effect at the tunnel junction[8,14]. The time-dependent modulation of the potential barrier was also calculated using the Simmons model. As shown in Figs. 2f and 2g, the potential barrier is coherently distorted by the enhanced THz electric field at the junction. For example, the barrier height is reduced to 0.98 eV whereas the barrier width decreases to 0.41 nm at the field strength of +5.3 V/nm. In contrast, a field strength of -2.0 V/nm produces less barrier shrinkage, with the height and width reduced to 1.78 eV and 0.75 nm, respectively. This potential asymmetry driven by the CEP-locked single-cycle THz electric field leads to unidirectional electron tunnelling through the junction within a sub-picosecond time scale.

By further increasing the THz electric field, we can implement a new regime for electron tunnelling that is inaccessible by conventional STM. The results are shown in Fig. 3a for the use of three different tips: two sharp nanotips (tips 1, 2) and one blunt tip (tip 3) as shown in the inset. The plots of the number of rectified electrons against the incident electric field exhibit different behaviours among the tips. However, after converting the incident electric field into the enhanced electric field, the curves exhibit almost the same behaviour (Fig. 3b), indicating that the tip geometry affects only the enhancement factor, and the sharp tip can tightly focus the THz electric field.

The striking feature in Fig. 3b is the strong saturation of the tunnelling electrons observed above the enhanced electric field of 6 V/nm, which was unexpected by the

conventional Simmons model. A recent self-consistent calculation[29] predicted a new regime that deviates from the Simmons model at extremely high voltages, the so-called "space-charge-limited" regime, in which an additional space charge potential plays an important role in limiting the current flow in the junction. In this calculation, the saturation of the tunnel currents occurred above 6 V/nm with a work function of 4.08 eV; these values are in reasonably good agreement with our results. Note that this regime cannot be realized with a DC bias voltage or near-infrared pulses, because the former and the latter easily damage the junction owing to Joule heating and high-energy photons, respectively[20]. Finally, we stress that an enhanced THz electric field of 16 V/nm was achieved at the junction, which is two times higher than the strongest THz field previously reported in a free space[30]. This spatially confined huge single-cycle THz electric field can coherently drive the motion of as many as ~300,000 electrons within a sub-picosecond time scale.

In summary, we have demonstrated the real-space coherent manipulation of electrons in a single tunnel junction. By utilizing CEP-controlled single-cycle THz electric fields, electron tunnelling can be induced either from a nanotip to a sample or vice versa. The extremely large field enhancement at the junction strongly modulates the potential barrier between a nanotip and sample, leading to the strong saturation of rectified electrons in a space-charge-limited regime. We believe that this concept provides a new platform for the ultrafast coherent control of electrons, and may inspire a new route towards designing future nanoelectronics. Furthermore, our CEP-controlled THz-STM with an extremely high electric field is expected to be a powerful tool for exploring the ultrafast nonlinear control of matter[22] at the atomic scale.

Figure captions

Figure 1 | Experimental setup for THz-STM. a, Schematic of the experimental setup. CEP-controlled single-cycle THz electric fields are focused onto the apex of a Pt/Ir nanotip with an incident angle of 75°. OAP, off-axis parabolic mirror; EOS, electro-optic sampling. **b**, Schematic illustration of π phase-shift of a THz electric field via the Gouy phase shift using a pair of spherical lenses. A pair of cylindrical lenses is used when a π/2 phase-shift is required. **c**, Schematic illustration of an electron (e^-)

tunnelling between a nanotip and a sample under the influence of a static electric field. The motion of electrons is coherently controlled by THz electric fields with different CEPs. **d**, Temporal profile of a single-cycle THz electric field (ϕ_{CEP} = 0) measured using the EOS. The inset shows the corresponding THz frequency spectrum. **e**, Pulse train generated by the THz electric field (ϕ_{CEP} = 0) without any DC bias. The feedback loop remained off during the measurement (setpoint: bias voltage V_s = 1 V; tunnel current I_s = 1 nA). The decay profile of each current pulse comes from the bandwidth of the amplifier used in the STM circuits.

Figure 2 | Effect of CEP on the motion of tunnelling electrons. a, Temporal profiles of single-cycle THz electric fields with different CEPs (ϕ_{CEP} = 0, π/2, and π). **b**, CEP dependence of tunnel current as a function of DC bias (V_s = 1 V, I_s = 0.5 nA). The spectra with ϕ_{CEP} = 0 and π are offset by ± 0.07 nA for clarity. **c**, Schematic illustration of the motion of electrons driven by THz electric fields with different CEPs. The orange and blue arrows show the tunnelling direction. **d**, Number of rectified electrons induced by a single THz pulse without DC bias as a function of the peak electric field (V_s = 1 V, I_s = 1 nA). The insets show the corresponding incident THz waveforms with different CEPs (ϕ_{CEP} = 0, π). The dashed curve shows the best fit obtained by the Simmons model. **e**, Potential barrier between nanotip (M_1) and sample (M_2) under a bias voltage of V, where s is the width of the gap between the tip and the sample. **f**, Time dependence of potential barrier under an enhanced THz electric field. **g**, Potential barriers at t = 5 and t = 5.7 ps, which are indicated by the dashed lines in **f**. The electron undergoes tunnelling in the smaller potential barrier at t = 5 ps rather than that at t = 5.7 ps, as shown by the thicker and thinner arrows, respectively. The thicker arrow indicates the higher probability of tunnelling.

Figure 3 | Current saturation under strong electric fields. a, Number of rectified electrons without DC bias as a function of incident electric field (ϕ_{CEP} = 0) for different tips (V_s = 1 V, I_s = 1 nA). Tips 1 and 2 (sharp) were fabricated by electrochemical etching, whereas tip 3 (blunt) was formed by mechanical cutting. Insets: SEM images of the sharp (top) and blunt (bottom) tips. **b**, Log-scale plot of number of rectified electrons as a function of the enhanced electric field at the tunnel junction. The

enhancement factor of tip 3 is 50,000 ± 200, which is two times smaller than that of the sharp nanotips. Error bars correspond to 95% confidence intervals.

Methods

Methods and any associated references are available in the online version of the paper.

References

1. Paulus, G. G. *et al.* Measurement of the phase of few-cycle laser pulses. *Phys. Rev. Lett.* **91**, 253004 (2003).

2. Corkum, P. B. & Krausz, F. Attosecond science. *Nat. Phys.* **3,** 381–387 (2007).

3. Schiffrin, A. *et al.* Optical-field-induced current in dielectrics. *Nature* **493,** 70–74 (2013).

4. Paasch-Colberg, T. *et al.* Solid-state light-phase detector. *Nat. Photon.* **8**, 214–218 (2014).

5. Luu, T. T. *et al.* Extreme ultraviolet high-harmonic spectroscopy of solids. *Nature* **521,** 498–502 (2015).

6. Hohenleutner, M. *et al.* Real-time observation of interfering crystal electrons in high-harmonic generation. *Nature* **523,** 572–575 (2015).

7. Krüger, M., Schenk, M. & Hommelhoff, P. Attosecond control of electrons emitted from a nanoscale metal tip. *Nature* **475,** 78–81 (2011).

8. Wimmer, L. *et al.* Terahertz control of nanotip photoemission. *Nat. Phys.* **10,** 432–436 (2014).

9. Piglosiewicz, B. *et al.* Carrier-envelope phase effects on the strong-field photoemission of electrons from metallic nanostructures. *Nat. Photon.* **8,** 37–42 (2014).

10. Caulfield, H. J. & Dolev, S. Why future supercomputing requires optics. *Nat. Photon.* **4,** 261–263 (2010).

11. Krausz, F. & Stockman, M. I. Attosecond metrology: from electron capture to future signal processing. *Nat. Photon.* **8,** 205–213 (2014).

12. Ward, D. R., Hüser, F., Pauly, F., Cuevas, J. C. & Natelson, D. Optical rectification and field enhancement in a plasmonic nanogap. *Nat. Nanotech.* **5,** 732–736 (2010).

13. Vincent, R., Klyatskaya, S., Ruben, M., Wernsdorfer, W. & Balestro, F. Electronic read-out of a single nuclear spin using a molecular spin transistor. *Nature* **488,** 357–60

(2012).

14. Yoshida, K., Shibata, K. & Hirakawa, K. Terahertz Field Enhancement and Photon-Assisted Tunneling in Single-Molecule Transistors. *Phys. Rev. Lett.* **115,** 138302 (2015).

15. Sharma, A., Singh, V., Bougher, T. L. & Cola, B. A. A carbon nanotube optical rectenna. *Nat. Nanotech.* **10,** 1027–1032 (2015).

16. Savage, K. J. *et al.* Revealing the quantum regime in tunnelling plasmonics. *Nature* **491,** 574–7 (2012).

17. Tan, S. F. *et al.* Quantum Plasmon Resonances Controlled by Molecular Tunnel Junctions. *Science* **343,** 1496–1499 (2014).

18. Bahk, Y.-M. *et al.* Electromagnetic Saturation of Angstrom-Sized Quantum Barriers at Terahertz Frequencies. *Phys. Rev. Lett.* **115,** 125501 (2015).

19. Cocker, T., Jelic, V. & Gupta, M. An ultrafast terahertz scanning tunnelling microscope. *Nat. Photon.* **7,** 620–625 (2013).

20. Grafström, S. Photoassisted scanning tunneling microscopy. *J. Appl. Phys.* **91,** 1717 (2002).

21. Hirori, H., Doi, A., Blanchard, F. & Tanaka, K. Single-cycle terahertz pulses with amplitudes exceeding 1 MV/cm generated by optical rectification in $LiNbO_3$. *Appl. Phys. Lett.* **98,** 091106 (2011).

22. Kampfrath, T., Tanaka, K. & Nelson, K. A. Resonant and nonresonant control over matter and light by intense terahertz transients. *Nat. Photon.* **7,** 680–690 (2013).

23. Yoshioka, K. *et al.* Terahertz-Field-Induced Nonlinear Electron Delocalization in Au Nanostructures. *Nano Lett.* **15,** 1036–1040 (2015).

24. Terada, Y., Yoshida, S., Takeuchi, O. & Shigekawa, H. Real-space imaging of transient carrier dynamics by nanoscale pump–probe microscopy. *Nat. Photon.* **4,** 869–874 (2010).

25. Yoshida, S. *et al.* Probing ultrafast spin dynamics with optical pump-probe scanning tunnelling microscopy. *Nat. Nanotech.* **9,** 588–593 (2014).

26. Feng, S. & Winful, H. G. Physical origin of the Gouy phase shift. *Opt. Lett.* **26,** 485–487 (2001).

27. Higuchi, T., Maisenbacher, L., Liehl, A., Dombi, P. & Hommelhoff, P. A nanoscale vacuum-tube diode triggered by few-cycle laser pulses. *Appl. Phys. Lett.* **106,** 051109

(2015).
28. Simmons, J. G. Generalized Formula for the Electric Tunnel Effect between Similar Electrodes Separated by a Thin Insulating Film. *J. Appl. Phys.* **34,** 1793–1803 (1963).
29. Zhang, P. Scaling for quantum tunneling current in nano- and subnano-scale plasmonic junctions. *Sci. Rep.* **5,** 9826 (2015).
30. Shalaby, M. & Hauri, C. P. Demonstration of a low-frequency three-dimensional terahertz bullet with extreme brightness. *Nat. Commun.* **5976,** 1–8 (2015).

Acknowledgements
This work was supported in part by the Grants-in-Aid for Scientific Research (Nos. 15H05734, 16H03820, 16H04001 and 16H06010) from the Japan Society for the Promotion of Science and the Ministry of Education, Culture, Sports, Science and Technology, and by Strategic Information and Communications R&D Promotion Programme (SCOPE #145003103) of Japan Ministry of Internal Affairs and Communications.

Author contributions
I.K., M.K., H.S. and J.T. conceived and coordinated this project. K.Y. designed and built the THz-STM set-up. K.Y. and Y.M. developed the intense THz generation system, and K.Y. and S.Y. constructed the operation program of the STM. K.Y. carried out the experiments and simulations with support from I.K., Y.M. and S.Y., and H.S., M.K. and J.T. contributed to the initial concept of the experiments. K.Y. and J.T. wrote this manuscript with contribution from all authors.

Additional information
Supplementary information is available in the online version of the paper. Reprints and permissions information is available online at www.nature.com/reprints. Correspondence and requests for materials should be addressed to J.T, I.K. and H.S.

Competing financial interests
The authors declare no competing financial interests.

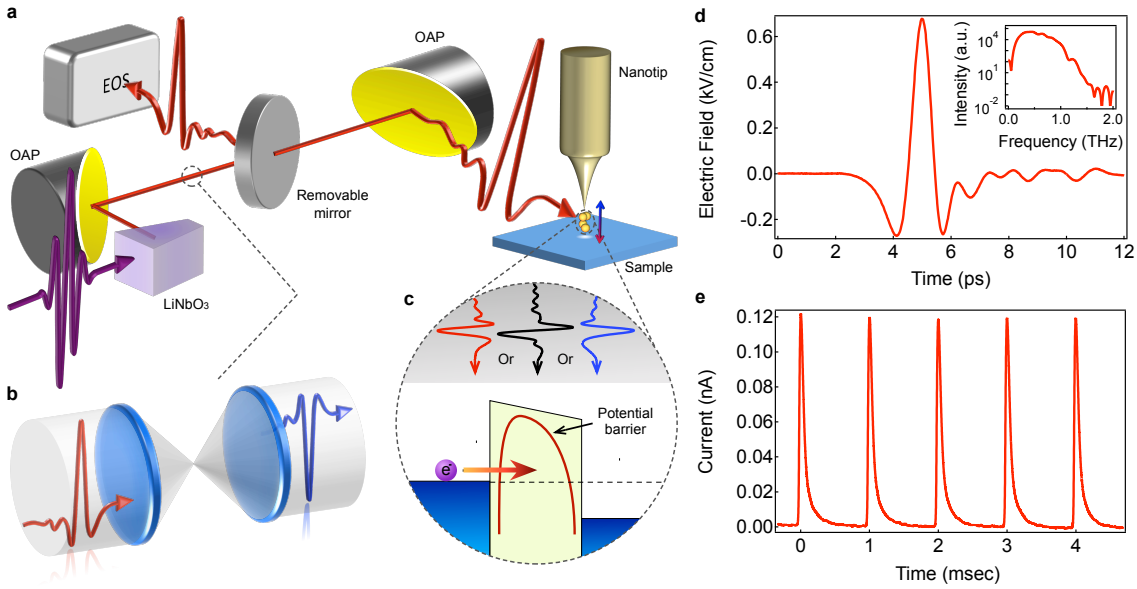
a
EOS
OAP
OAP
Nanotip
Removable
mirror
LiNbO3
Sample
b
c
Or
Or
Potential
barrier
e
d
Electric Field (kV/cm)
0.6
0.4
0.2
0.0
-0.2
0
2
4
6
8
10
12
Time (ps)
Intensity (a.u.)
Frequency (THz)
e
Current (nA)
0.12
0.10
0.08
0.06
0.04
0.02
0.00
0
1
2
3
4
Time (msec)

Figure 1

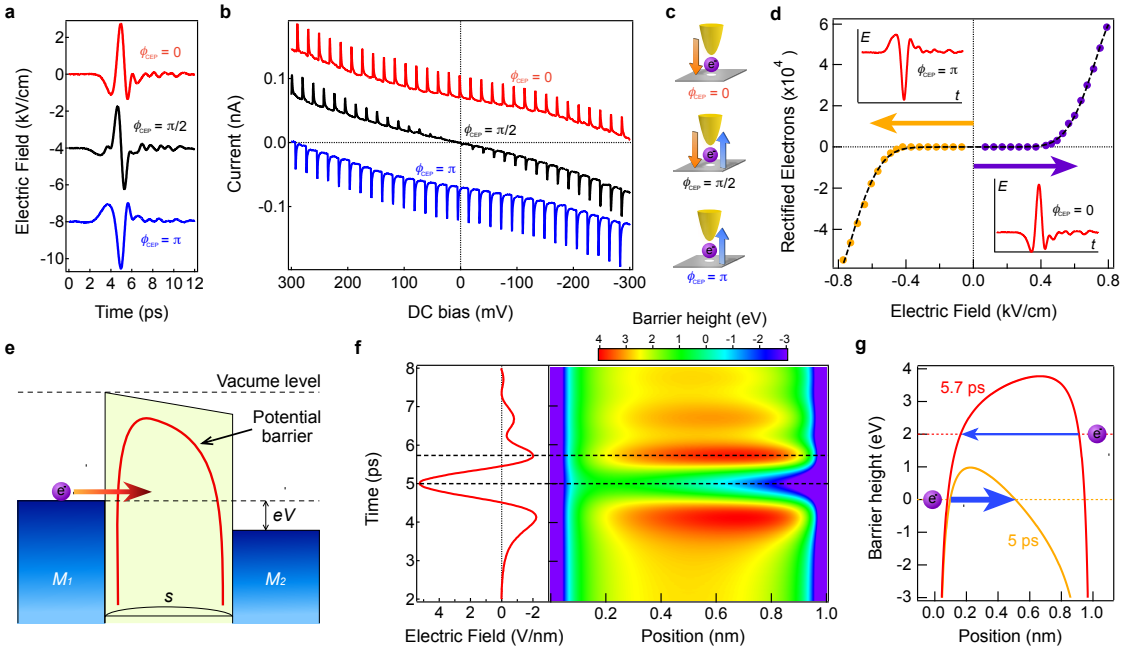
a
Electric Field (kV/cm)
Time (ps)
b
Current (nA)
DC bias (mV)
c
d
Rectified Electrons (x10^4)
Electric Field (kV/cm)
e
Vacume level
Potential barrier
eV
M1
M2
s
f
Barrier height (eV)
Time (ps)
Electric Field (V/nm)
Position (nm)
g
5.7 ps
5 ps
Barrier height (eV)
Position (nm)

Figure 2

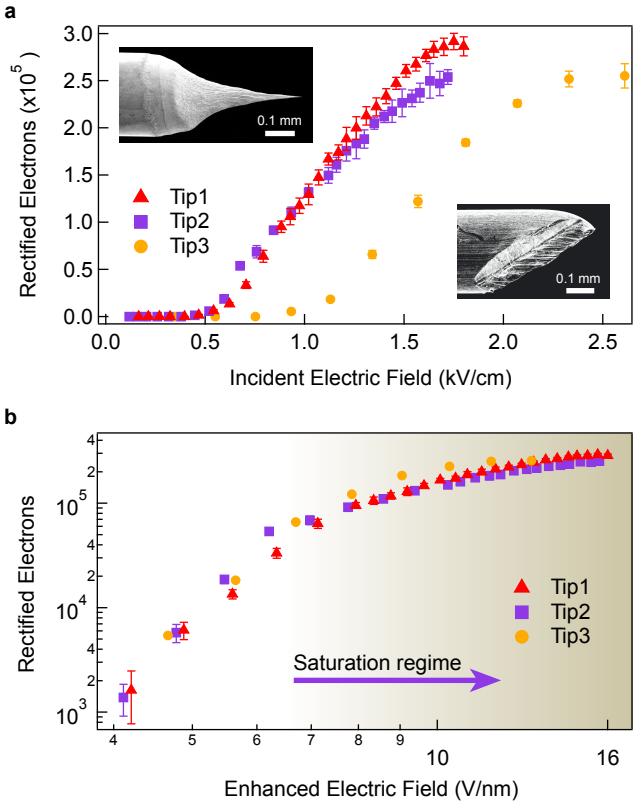
a
Rectified Electrons (x10^5)
3.0
2.5
2.0
1.5
1.0
0.5
0.0
0.0
0.5
1.0
1.5
2.0
2.5
Incident Electric Field (kV/cm)
0.1 mm
0.1 mm
Tip1
Tip2
Tip3
b
Rectified Electrons
10^5
10^4
10^3
4
5
6
7
8
9
10
16
Enhanced Electric Field (V/nm)
Saturation regime
Tip1
Tip2
Tip3

Figure 3

Real-space coherent manipulation of electrons in a single tunnel junction by single-cycle terahertz electric fields

Katsumasa Yoshioka[1], Ikufumi Katayama[1], Yasuo Minami[1], Masahiro Kitajima[1,2], Shoji Yoshida[3], Hidemi Shigekawa[3], and Jun Takeda[1]

[1]Department of Physics, Graduate School of Engineering,
Yokohama National University, Yokohama 240-8501, Japan
[2]LxRay Co. Ltd., Nishinomiya 663-8172, Japan
[3]Faculty of Pure and Applied Sciences,
University of Tsukuba, Tsukuba 305-8571, Japan

Supplementary Information

I-a. Scanning tunnelling microscope

A commercial STM (Digital Instruments, Nanoscope E), which has excellent stability in air, was used in this study. Sharp nanotips were fabricated by electrochemical etching of a Pt/Ir (80/20%) wire with a diameter of 0.3 mm, while blunter tips were obtained by pulling the wire with pliers. The formation of the tip apex was confirmed using a scanning electron microscope (SEM) as shown in Fig. S1a. HOPG was freshly cleaved before the measurements to obtain a clean surface, and its atomically flat surface was confirmed using the STM as shown in Fig. S1b. Figure S1c shows a tunnel current pulse with a response time of 63 ± 1 μs generated by a single THz pulse. This response time corresponds to the bandwidth (15 kHz) of a current amplifier incorporated in the STM circuits. Since the bandwidth is much greater than the repetition rate (1 kHz) of THz pulses, the time integration of a current pulse gives the number of rectified electrons driven by a single THz pulse through the junction; the number of rectified electrons, N, was calculated by $N = \int (I(t)/e)\, dt$, where $I(t)$ is the tunnel current and e is the elementary charge.

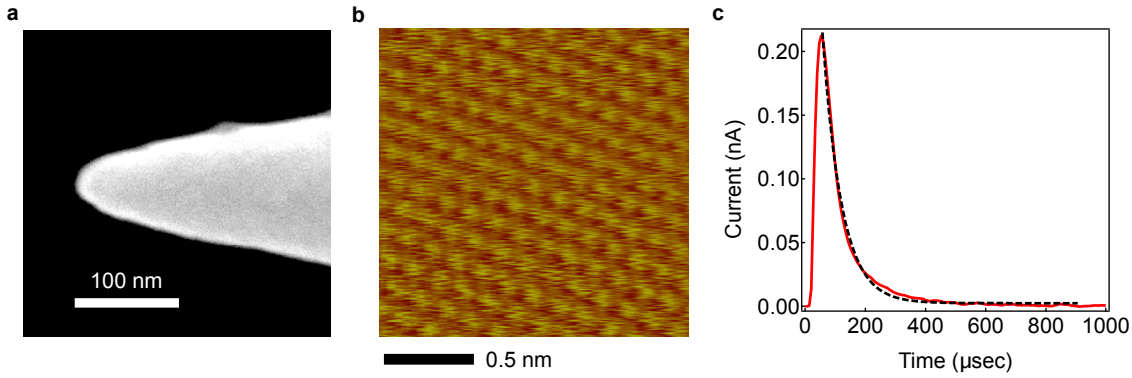

Figure S1 | a, SEM image of a sharp nanotip with a tip apex diameter of 40 nm. **b**, STM image of HOPG with atomic resolution. **c**, Typical current pulse generated by a single THz pulse. The dashed curve shows the best fit obtained using a single exponential function with a response time of 63 ± 1 μs, which corresponds to the bandwidth of the current amplifier incorporated in the STM.

I-b. Experimental setup for the THz-STM

Figure S2 shows our experimental setup. As a light source, we employed a Ti:sapphire regenerative amplifier with a repetition rate of 1 kHz, a pulse duration of 130 fs, and a centre wavelength of 800 nm. Intense single-cycle THz electric field transients were generated using a $LiNbO_3$ prism in a tilted-pulse-front configuration [1]. The generated THz pulses were collimated by a gold-coated off-axis parabolic mirror (PM1), and the field strength was tuned by a pair of wire grid polarizers. To produce the THz pulses with a CEP of π or π/2, we set either a pair of spherical or cylindrical Tsurupica lenses, respectively, in the optical pathway. The waveform-controlled THz pulses were then guided into one of two paths by tuning a removable Au-coated mirror: one was used for characterizing the THz pulses by electro-optic sampling (EOS) and the other was used for delivering the THz pulses to a tunnel junction of the STM. For the EOS, a 2 mm-thick ZnTe (110) crystal was used as an EO crystal. The field strength was evaluated by assuming an electro-optic coefficient of r_{41} = 3.9 pm/V and the refractive indices of $n_{800\text{nm}}$ = 2.86 and n_{THz} = 3.19. To accurately characterize the THz waveform at the junction, the same off-axis parabolic mirrors (PM2 and PM3) with 4-inch focal length and 2-inch diameter were used to focus the THz pulses. The resulting beam diameter at the STM junction and the EO crystal was 1.2 mm. The THz tunnel current was recorded by a digital oscilloscope via the STM circuits. Note that

intense THz electric fields with a repetition rate lower than the bandwidth of the circuits were used in our system. Therefore, we could sensitively observe the tunnel current as a pulse train in real-time using a conventional oscilloscope (see Figs. 1e and 2b in the main text).

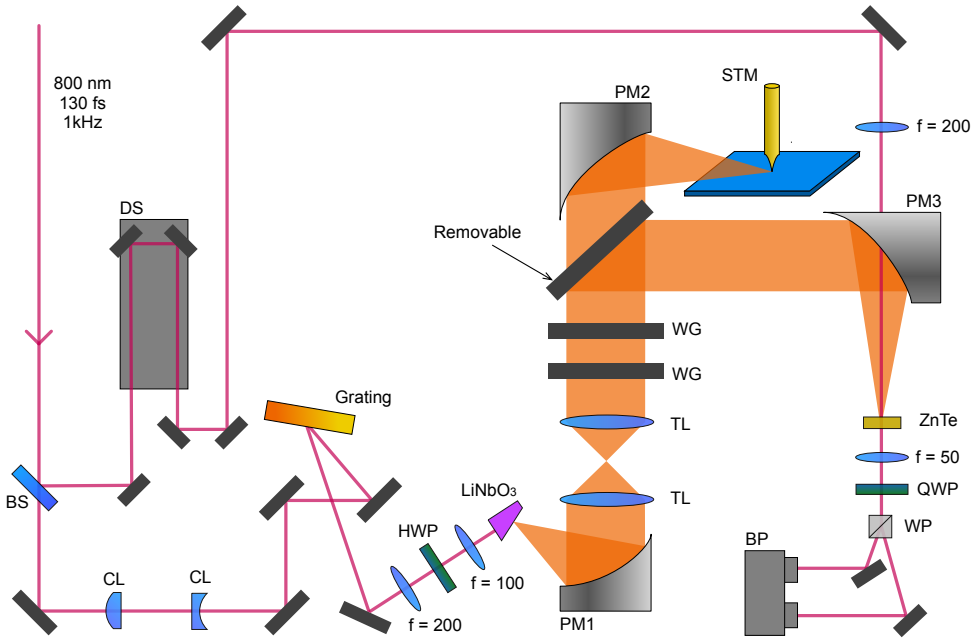

Figure S2 | Experimental setup for THz-STM. BS: beam splitter, DS: delay stage, CL: cylindrical lens, HWP: half-wave plate, PM: parabolic mirror, TL: Tsurupica lens, WG: wire grid polarizer, QWP: quarter-wave plate, WP: Wollaston prism, BP balanced photodiode.

II. DC bias dependence of the THz-induced electron tunnelling

Under a DC bias, the total electric field at a tunnel junction with THz electric fields can be expressed as $E_{THz} + E_{DC}$. To reveal the DC bias dependence of the tunnel current as shown in Fig. 2b, we performed simulations based on the Simmons model (see Supplementary Information III). Using the temporal profile of the THz electric fields ($\phi_{CEP} = 0$) with different DC biases (Fig. S3a), the tunnel current and the number of rectified electrons at the junction were obtained as a function of time (Figs. S3b and 3c). Note that the tunnel current increases nonlinearly only around the peak THz electric field ($t \sim 3$ ps) with increasing DC bias, leading to a rapid increase in the number of

rectified electrons within a sub-picosecond time scale. The reverse polarity of the tunnel current and rectified electrons was expected when applying a THz electric field with $\phi_{CEP} = \pi$. Reflecting the asymmetric single-cycle cosinusoidal THz waveform, nearly all of the electrons contributed to the unidirectional tunnelling.

In a similar manner, the simulations were performed using the temporal profile of the THz electric field ($\phi_{CEP} = \pi/2$) with different DC biases (Fig. S3d). Reflecting the sinusoidal electric field, the tunnel current flows for both polarities. Upon applying a DC bias, however, the tunnel current becomes asymmetric owing to the strong nonlinearity of the tunnel junction (Fig. S3e). As a result, after the THz electric field has passed through the junction ($t \sim 5$ ps), not only the number of rectified electrons but also their direction can be tuned by the DC bias: electron tunnelling is induced from the nanotip to the sample under a positive DC bias, and in the opposite direction under a negative DC bias. These calculations are in good agreement with the experimental results shown in Fig. 2b.

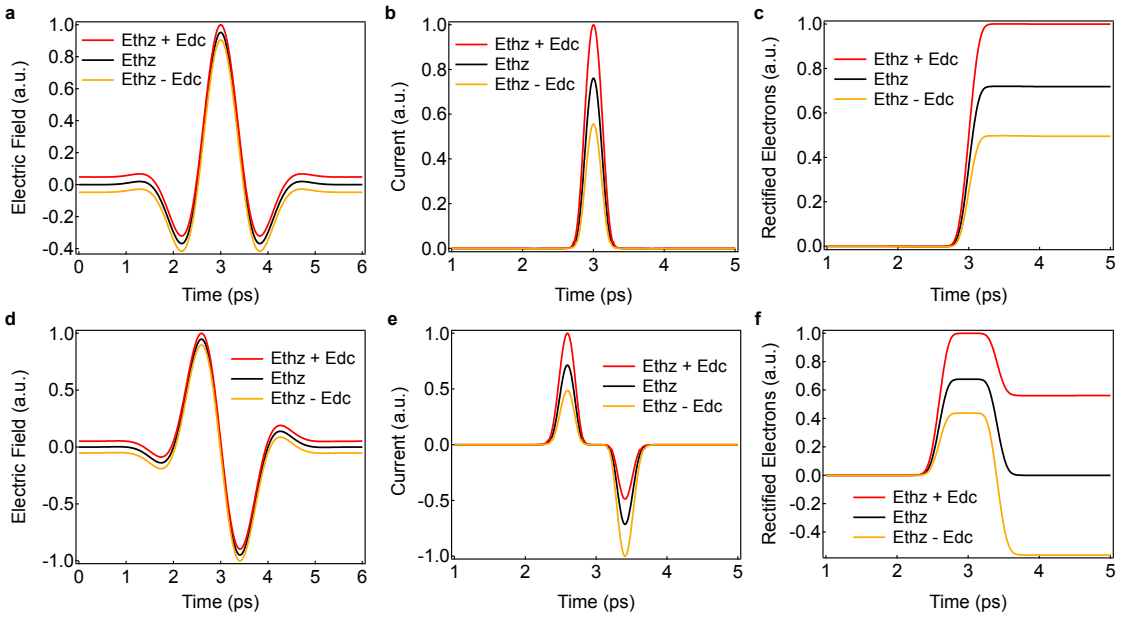

Figure S3 | a-c, Results of simulations with a THz electric field ($\phi_{CEP} = 0$). **a**, Calculated THz electric fields with different DC biases. **b**, Tunnel currents obtained using the Simmons model. **c**, Number of rectified electrons obtained by integration of the tunnel currents in **b**. **d-f**, Corresponding results of simulations with a THz electric field ($\phi_{CEP} = \pi/2$).

III. Simmons model calculation

Several theoretical models have been proposed to understand the electron transport at a tunnel junction [2-7]. Ward *et al*. calculated electron transmission curves as a function of energy in an attempt to explain the electron transport at a metal tunnel junction subjected to a cw visible laser having high photon energy (1.58 eV) [2]. Since their calculation was based on the Landauer approach, the validity of this model is only limited to the linear regime. This model is therefore not suitable for our THz-STM experiments with extremely nonlinear behaviour. The Tersoff and Humann model has been widely utilized to describe the electron transport at a tunnel junction with 3D characteristics [3,4]. However, this model also assumes a low-voltage regime, making it inapplicable to our experiments. Another approach is the extended Simmons model [5], in which both the electrostatic and image potentials are modified to describe a STM junction with 3D characteristics. However, notational, geometrical, and electrical inconsistencies in the descriptions of the hyperboloidal electrodes and the electrostatic potential were pointed out by Ley-Koo [6].

Although the basic Simmons model is suitable for a tunnel junction with planar plates [7], we believe that this model is one of the better choices for understanding the physics underlying our THz-STM experiments with extremely nonlinear behavior, which is considerably different from that in conventional STM experiments. Because the photon-assisted tunnelling is negligible owing to the low energy of the THz pulses (~ 4.2 meV), the electron transmission might be accurately calculated using the WKB approximation in the Simmons model. Indeed, the results of THz-STM experiments with weak electric fields have been qualitatively explained by the Simmons model [8].

According to the above reasons, we used the Simmons model [7] to analyse the motion of electrons in a tunnel junction, which is generally applicable to a DC condition. Because the typical time required for electron tunnelling is less than 1 fs [9,10] and much shorter than the period of the driving field, the THz electric field transient acts as a quasi-static field. Therefore, the Simmons model can also be applied to our experimental results.

The potential barrier between a nanotip and sample (Fig. S4a) is expressed by considering a rectangular potential barrier, an external bias voltage, and an image potential as follows;

$$\varphi(x) = \varphi_0 - \frac{eV}{s}x + V_i(x),$$

where φ_0 is the effective work function of the junction, V is the applied bias voltage across the gap, s is the gap width, and $V_i(x)$ is the image potential. The $V_i(x)$ is given by

$$V_i(x) = \left(-\frac{e^2}{8\pi\varepsilon}\right)\left[\frac{1}{2x} + \sum_{n=1}^{\infty}\left\{\frac{ns}{[(ns)^2 - x^2]}\right\} - \frac{1}{ns}\right],$$

where ε is the permittivity of the gap. Here, we used an approximated image potential given by

$$V_i(x) = -\frac{1.15\lambda s^2}{x(s-x)},$$

where

$$\lambda = \frac{e^2 ln2}{16\pi\varepsilon s},$$

which is a good approximation to the true image potential. Note that the V_i used here is half that in the original Simmons equation, which included an error as pointed out by Miskovsky *et al.* [11]. We also notify that the experimental results cannot be explained without considering the image potential as shown in Fig. S4b. Using this method, the tunnel current J is given by

$$J = \alpha J_0\left\{\bar{\varphi}\exp(-A\bar{\varphi}^{\frac{1}{2}}) - (\bar{\varphi} + eV)\exp\left[-A(\bar{\varphi} + eV)^{\frac{1}{2}}\right]\right\},$$

with $J_0 = e/2\pi h\Delta s^2$ and $A = (4\pi\Delta s/h)(2m)^{\frac{1}{2}}$, where $\bar{\varphi}$ is the mean barrier height, $\Delta s(= s_1 - s_2)$ is the effective barrier width, m is the electron mass, h is Planck's constant, and α is a scaling parameter that accounts for the density of states and the effect of the geometry of the tip apex. The mean barrier height is given by

$$\bar{\varphi} = \frac{1}{\Delta s}\int_{s_2}^{s_1} V_i(x)\,dx,$$

where s_1 and s_2 are the real roots of the cubic equation

$$\varphi_0 - \frac{eV}{s}x - \frac{1.15\lambda s^2}{x(s-x)} = 0.$$

The resulting best fit with an effective work function of 3.8 ± 0.1 eV, a gap width of 1.00 ± 0.01 nm, and an enhancement factor of 100,000 ± 10,000, shown by the dashed curve in Fig. 2d, is in good agreement with the experimental result. The obtained gap width is a reasonable value for a typical STM parameter. The effective work function of 3.8 ± 0.1 eV is slightly lower than that of the nanotip and the sample [12,13] (~ 5 eV) because of the presence of adsorbates in the air [14]. The estimated enhancement factor indicates an extremely large THz electric field at the junction and is in reasonably good agreement with that at a single-molecule tunnel junction subjected to monochromatic cw-THz radiation [15], whose value is on the order of λ_{THz}/d (λ_{THz} is the THz wavelength and d the nm-scale gap width; 100 (μm)/ 1 (nm) = 100,000).

To further confirm the validity of the estimated parameters, i.e., the effective work function, the gap width and the field enhancement factor, we carried out two I-Z (current vs. distance) and DC I-V (current vs. voltage) measurements. Figure S5a shows the observed current as a function of the change in the tip-surface distance to evaluate the work function. The mean barrier height $\bar{\varphi}$ was estimated to be 3.3 ± 0.1 eV under the setpoint bias voltage of 1 V. The work function φ_0 was therefore determined to be 3.8 ± 0.1 eV by taking account of the fact that $\bar{\varphi} = (\varphi_0 - eV/2)$. On the other hand, as shown in Fig. S5b, the gap width was experimentally estimated to be 0.85 ± 0.17 nm by driving the tip into the HOPG sample. These values are in reasonably good agreement with those obtained from the Simmons model. Finally, we performed DC I-V measurement under a high-voltage regime to directly determine the field enhancement factor [16]. The upper limit of the DC voltage was 3.2 V because of the damage threshold of the HOPG sample [17]. The THz I-V measurement was also carried out under low THz electric fields (0.3-0.4 kV/cm) to combine the results of the two I-V experiments i.e., the DC I-V experiment and the THz I-V experiment under high electric fields shown in Fig. 2d. Here, the THz I-V data were reproduced from the THz-field-induced current data (as typically shown in Fig. 2d) using the THz waveforms experimentally obtained by EOS, and the obtained field enhancement factor was 100,000 ± 10,000. As shown in Fig. S5c, the three experimental results smoothly overlap, indicating that the obtained field enhancement factor is in fairly good agreement with that estimated from the Simmons model.

Using the Simmons model, we were able to obtain reasonable values for various parameters, strongly indicating that this model is satisfactory for understanding the physics underlying our experimental results. We expect that our experimental results will accelerate the establishment of elaborate theoretical models that can be utilized to quantitatively investigate the nonlinear transport of electrons at a junction in an extremely nonlinear regime.

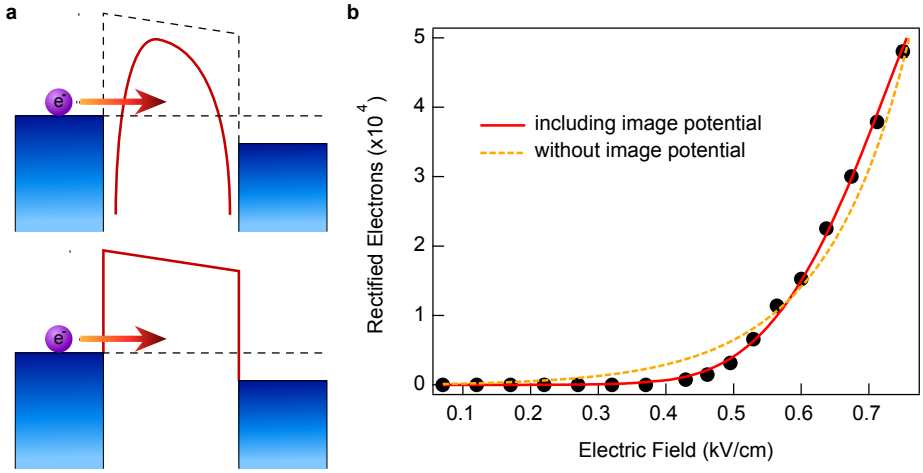

Figure S4 | a, Schematic illustration of the potential barrier between a nanotip and a sample. The upper and lower images show the barrier with and without the image potential, respectively. **b**, Number of rectified electrons induced by a single THz pulse without DC bias as a function of the peak electric field (ϕ_{CEP} = 0). The solid line shows the best fit obtained by the Simmons model with the image potential, while the dashed curve indicates that without the image potential.

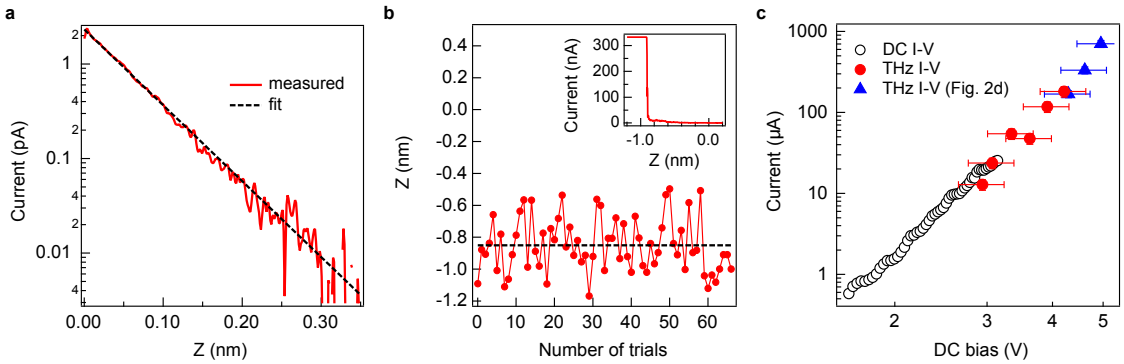

Figure S5 | a, Measured I-Z curve (setpoint: bias voltage V_s = 1 V, tunnel current I_s = 2.5 pA). The data were fitted using $I = exp(-1.025\sqrt{\bar{\varphi}}\,Z)$ with a mean barrier height of $\bar{\varphi}$ = 3.3 ± 0.1 eV. **b**, Gap measured by driving the tip into the graphite (V_s = 1 V, I_s = 1 nA). The inset shows a typical I-Z curve. The rapid increase in the current indicates the point of contact. The gap width was determined to be 0.85 ± 0.17 nm. **c**, Log-log plot of I-V data obtained from the DC I-V and THz I-V measurements (V_s = 1 V, I_s = 1 nA). The THz I-V data were reproduced from the THz-field-induced current data using the THz waveforms experimentally obtained by EOS, and the field enhancement factor was 100,000 ± 10,000.

References

[1] Hirori, H., Doi, A., Blanchard, F. & Tanaka, K. Single-cycle terahertz pulses with amplitudes exceeding 1 MV/cm generated by optical rectification in $LiNbO_3$. *Appl. Phys. Lett.* **98,** 091106 (2011).

[2] Ward, D. R., Hüser, F., Pauly, F., Cuevas, J. C. & Natelson, D. Optical rectification and field enhancement in a plasmonic nanogap. *Nat. Nanotech.* **5,** 732–736 (2010).

[3] Tersoff, J. & Hamann, D. R. Theory and application for the scanning tunneling microscope. *Phys. Rev. Lett.* **50**, 1998–2001 (1983).

[4] Tersoff, J. & Hamann, D. R. Theory of the scanning tunneling microscope. *Phys. Rev. B* **31**, 805–813 (1985).

[5] Seine, G. *et al.* Tip-to-surface distance variations vs voltage in scanning tunneling microscopy. *Phys. Rev. B* **60**, 11045–11050 (1999).

[6] Ley-Koo, E. Comment on 'Tip-to-surface distance variations vs voltage in scanning tunneling microscopy'. *Phys. Rev. B* **65**, 077401 (2002).

[7] Simmons, J. G. Generalized Formula for the Electric Tunnel Effect between Similar Electrodes Separated by a Thin Insulating Film. *J. Appl. Phys.* **34,** 1793–1803 (1963).

[8] Cocker, T. L. *et al.* An ultrafast terahertz scanning tunnelling microscope. *Nat. Photon.* **7,** 620–625 (2013).

[9] Zhang, P. Scaling for quantum tunneling current in nano- and subnano-scale plasmonic junctions. *Sci. Rep.* **5,** 9826 (2015).

[10] Shafir, D. *et al.* Resolving the time when an electron exits a tunnelling barrier. *Nature* **485,** 343–346 (2012).

[11] Miskovsky, N. M., Cutler, P. H., Feuchtwang, T. E. & Lucas, A. A. The multiple-image interactions and the mean-barrier approximation in MOM and MVM tunneling junctions. *Appl. Phys. A Solids Surfaces* **27,** 139–147 (1982).

[12] Skriver, H. L. & Rosengaard, N. M. Surface-Energy and Work Function of Elemental Metals. *Phys. Rev. B* **46,** 7157–7168 (1992).

[13] Suzuki, S., Bower, C., Watanabe, Y. & Zhou, O. Work functions and valence band states of pristine and Cs-intercalated single-walled carbon nanotube bundles. *Appl. Phys. Lett.* **76,** 4007 (2000).

[14] Chen, C. J. Introduction to Scanning Tunneling Microscopy (Oxford Univ. Press, 1993).

[15] Yoshida, K., Shibata, K. & Hirakawa, K. Terahertz Field Enhancement and

Photon-Assisted Tunneling in Single-Molecule Transistors. *Phys. Rev. Lett.* **115,** 138302 (2015).

[16] Kim, J.-Y. *et al.* Terahertz Quantum Plasmonics of Nanoslot Antennas in Nonlinear Regime. *Nano Lett*. **15**, 6683–6688 (2015).

[17] Shedd, G. M. & Russell, P. E. The scanning tunneling microscope as a tool for nanofabrication. *Nanotechnology* **1**, 67–80 (1990).